Medical Engineering and Physics 66 (2019) 40–46

Contents lists available at ScienceDirect

Medical Engineering and Physics

journal homepage: www.elsevier.com/locate/medengphy

A comparison of density–modulus relationships used in finite element modeling of the shoulder

Nikolas K. Knowles[a,c,e], G. Daniel G. Langohr[b,c,e], Mohammadreza Faieghi[a], Andrew J. Nelson[d,e,f], Louis M. Ferreira[b,c,e,*]

[a] School of Biomedical Engineering, The University of Western Ontario, London, ON, Canada
[b] Department of Mechanical and Materials Engineering, The University of Western Ontario, London, ON, Canada
[c] Roth|McFarlane Hand and Upper Limb Centre, Bioengineering Laboratory, Surgical Mechatronics Laboratory, St. Josephs Health Care, 268 Grosvenor St., London, ON, Canada
[d] Department of Anthropology, The University of Western Ontario, London, ON, Canada
[e] Collaborative Training Program in MSK Health Research, and Bone and Joint Institute, The University of Western Ontario, London, ON, Canada
[f] Department of Chemistry, The University of Western Ontario, London, ON, Canada

ARTICLE INFO

Article history:
Received 6 April 2018
Revised 29 November 2018
Accepted 10 February 2019

Keywords:
Finite-element analysis
Micro-CT
QCT
Density–modulus

ABSTRACT

Subject- and site-specific modeling techniques greatly improve the accuracy of computational models derived from clinical-resolution quantitative computed tomography (QCT) data. The majority of shoulder finite element (FE) studies use density–modulus relationships developed for alternative anatomical locations. As such, the objectives of this study were to compare the six most commonly used density–modulus relationships in shoulder finite element (FE) studies. To achieve this, ninety-eight (98) virtual trabecular bone cores were extracted from uCT scans of scapulae from 14 cadaveric specimens (7 male; 7 female). Homogeneous tissue moduli of 20 GPa, and heterogeneous tissue moduli scaled by CT-intensity were considered. Micro finite element models (μ-FEMs) of each virtual core were compressively loaded to 0.5% apparent strain and apparent strain energy density (SED_{app}) was collected. Each uCT virtual core was then co-registered to clinical QCT images, QCT-FEMs created, and each of the 6 density–modulus relationships applied ($6 \times 98 = 588$ QCT-FEMs). The loading and boundary conditions were replicated and SED_{app} was collected and compared to μ-FEM SED_{app}. When a homogeneous tissue modulus was considered in the μ-FEMs, SED_{app} was best predicted in QCT-FEMs with the density–modulus relationship developed from pooled anatomical locations (QCT-FEM $SED_{app} = 0.979$μ-FEM $SED_{app} + 0.0066$, $r^2 = 0.933$). A different density–modulus relationship best predicted SED_{app} (QCT-FEM $SED_{app} = 1.014$μ-FEM $SED_{app} + 0.0034$, $r^2 = 0.935$) when a heterogeneous tissue modulus was considered. This study compared density–modulus relationships used in shoulder FE studies using an independent computational methodology for comparing these relationships.

1. Introduction

Clinical-computed tomography (CT) scans are commonly performed for diagnostics and surgical planning of upper limb orthopaedic surgical procedures. Improvements in surgical procedures, implant designs, understanding of joint biomechanics, and pathologic conditions can be elucidated using clinical-resolution-derived computational finite element models (FEMs). As initial input to these models a constitutive relationship must be chosen that relates the CT-intensity to the bones' mechanical properties, to ensure that the resulting model is an accurate representation of the bone being modeled.

These density–modulus relationships have been shown to result in clinical-resolution-derived whole-bone FEMs that are highly correlated with experimental results ($R^2 > 0.90$) [1,2]. These relationships are thought to be site-specific, with anatomic site- and subject-specific modeling parameters shown to greatly improve the accuracy of clinical-resolution-derived FEMs [3–6]. However, it is common for relationships developed for one anatomic site, such as the hip, to be used in another, due to a paucity of established relationships. Pooling relationships from multiple anatomic sites to improve the modeling of mechanical properties in alternative sites

* Corresponding author at: Roth|McFarlane Hand and Upper Limb Centre, Bioengineering Laboratory, St. Josephs Health Care, 268 Grosvenor St. London, ON, Canada.
E-mail address: Louis.Ferreira@sjhc.london.on.ca (L.M. Ferreira).

https://doi.org/10.1016/j.medengphy.2019.02.005
1350-4533/

is one approach to cover a greater density range. However, this method neglects site-specific trabecular architecture, the local distribution of bone, and the geometric contributions from the cortical structure of whole-bones.

Anatomic site-specific linear isotropic density–modulus relationships are commonly used in biomechanics research for accurate material mapping in FEMs derived from commercially available (Mimics, Materialise, Leuven, BE.; Simpleware, Synopsys, Mountain View, CA, USA) and open source (BoneMat) software, making these relationships essential to FEM development. A large number of density–modulus relationships exist within the literature [7], with relationships primarily developed by testing physical trabecular and/or cortical bone specimens. However, when mechanically testing specimens, variations in experimental testing protocols have resulted in large systematic errors due to end-artifacts, specimen geometry, misrepresented boundary conditions, and the loss of load-carrying capacity of outer trabeculae due to coring [7–9]. To improve model accuracy and reduce these errors, computational μ-FEMs that account for mineral heterogeneity [10–15] may provide a robust method of density–modulus development.

A computational methodology has recently been reported that uses μ-FEMs and co-registered QCT-FEMs to compare the loading of trabecular bone cores [16]. This methodology eliminates some of the errors associated with traditional experimental mechanical testing of trabecular bone cores [17] and allows for the use of identical boundary conditions across models. Consistent with previous work, this methodology uses apparent strain energy density (SED_{app}) to compare multi-resolution modeling of trabecular bone [16,18]. Accounting for trabecular tissue heterogeneity at the micro-level has been shown to improve μ-FEM accuracy by allowing for a more accurate representation of trabecular bending stiffness [10–13,15]. Computationally, this is represented as a heterogeneous distribution of varying tissue modulus and is consistent with studies that have illustrated variations in trabecular tissue density superficially and at the core due to trabecular bone remodeling [19,20].

Six relationships are commonly used in shoulder FE studies [21–26], with only a single study having used scapular trabecular bone samples [22] for development. Shoulder FE studies lack experimental validation of the FE results, limiting the ability to translate outcomes and compare studies. This study compares these six relationships on the ability to predict SED_{app} in μ-FEMs derived from glenoid trabecular bone.

2. Materials and methods

2.1. Micro finite element model generation

Fourteen full-arm cadaveric specimens were obtained (7 male; 7 female; mean age 67 ± 8 years). The scapula was removed and denuded of all soft tissues. The glenoid fossa of each scapula was scanned with a micro-computed tomography scanner (Nikon XT H 225 ST, Nikon Metrology, NV, 95 kVp, 64 μA, 3141 projections, 1000 ms exposure). To include the entire glenoid structure in all scans from the largest to the smallest specimen, a fixed spatial resolution of 32 μm was used. As recommended for numerical convergence in subsequent μ-FEMs, this spatial resolution was less than one-fourth the mean trabecular thickness [27,28]. The images were exported as 16-bit Digital Imaging and Communications in Medicine (DICOM) format, and loaded to medical imaging software (Mimics, V.20.0, Materialise, Leuven, BE).

The raw images were filtered with a Gaussian filter ($\sigma = 1.25$, support = 2) to remove high frequency noise. A specimen-specific threshold was used to separate bone from the surrounding marrow, preserving trabecular geometry [29]. A three-dimensional stereolithography (STL) model was created and transferred to 3-Matic (V.12.0, Materialise, Leuven, BE). Volumes of interest (VOIs) with 5 mm edge length and 10 mm in length were placed medial to the glenoid articular surface subchondral bone. This size was chosen for consistency between the smallest and largest specimens, while maintaining the recommended 2:1 aspect ratio [7]. A maximum number of VOIs were placed in each specimen to ensure only glenoid vault trabecular bone was removed, resulting in 98 'virtual cores' among the 14 specimens. The 3D morphometric measurements for the cores had an average bone volume fraction (bone volume/total volume (BV/TV)) of 0.25 ± 0.08 (range: 0.10–0.51), trabecular thickness (Tb.Th*) of 0.26 ± 0.05 (range 0.17–0.40), trabecular separation (Tb.Sp*) of 0.80 ± 0.13 (range: 0.29–1.03), and a trabecular number (Tb.N*) of 0.93 ± 0.23 (range: 0.53–1.52) (Skyscan CTAn, Bruker micro-CT, Kontich, BE).

Each VOI was transferred back to Mimics and registered to the DICOM images, to associate each VOI with the corresponding grayscale intensity of the contained voxels. Region growing with 6-connectivity was used to ensure connected voxels. The central voxel coordinates and associated grayvalues were exported and custom code was used for direct conversion to eight node hexahedral elements [30]. Two tissue moduli cases were considered in μ-FEM development: a homogeneous tissue modulus, and a heterogeneous tissue modulus. In the former, all elements were assigned a uniform modulus of 20 GPa. In the latter, an element-wise material mapping was performed that used each voxel's grayvalue and a quantitative linear mapping to a reference modulus of 20 GPa, with a slope factor of 1.4 [13]. This resulted in a tissue modulus ranging from 4.3 to 21.5 GPa (16.9–39.2% coefficient of variation (COV)), and mean tissue modulus of 9.8 ± 1.0 GPa for all 98 heterogeneous μ-FEMs.

Following the methods described by Knowles et al. [16], the nodes of the bottom face of the resulting linear-isotropic homogeneous (98 μ-FEMs) and heterogeneous (98 μ-FEMs) were fully constrained, with the top nodes constrained to compressive only loading of 0.5% apparent strain [31] (Abaqus V.6.14, Simulia, Providence, RI, USA). Custom Matlab (Mathworks Inc., Natick, MA, USA) code generated the Abaqus input file, ensuring identical boundary conditions and loads between models. The apparent strain energy density (SED_{app}) was calculated for each of the 196 μ-FEMs.

2.2. Quantitative computed tomography (QCT) finite element model generation

The 14-cadaveric scapulae were also scanned with a clinical multi-slice CT-scanner (GE Discovery CT750 HD, Milwaukee, WI, USA, 120 kVp, 200 mAs, 320 mm FOV, 0.625 mm isotropic voxels, BONEPLUS convolution kernel). A liquid dipotassium phosphate (K_2HPO_4) calibration phantom (QCT Pro, Mindways Software Inc., Austin, TX, USA) was scanned with each specimen to provide a consistent density scaling reference among specimens (g_{K2HPO4}/cm^3). The DICOM images were loaded into Mimics, a 3D STL model was generated and transferred to 3-Matic. The QCT-model was co-registered to the μ-CT model using iterative closest points fitting. The previously placed uCT VOIs were duplicated and transformed to the QCT coordinate system using the coordinate transform between the two models. Each QCT VOI was transferred back to Mimics and registered to the DICOM images. The VOI size is evenly divisible by the QCT voxel dimensions, ensuring partial volume effects are eliminated during registration.

Custom-written Matlab code generated linear-isotropic models with eight-node hexahedral elements [30] and generated the Abaqus input file, with identical boundary and loading conditions to the μ-FEMs. The code was also used to implement each of the six non-linear density–modulus relationships used in shoulder finite element (FE) studies (Table 1). These relationships were

Table 1
Density–modulus relationships used in scapular FE studies.

	$E=\alpha\rho^{\beta}$					
Reference	Density measure (ρ)	Density range (g/cm^3)	Anatomic location	α	β	r^2
Morgan et al. [21]	Apparent	(0.09–0.75)	Pooled	8920	1.83	0.88
Morgan et al. [21]	Apparent	(0.26–0.75)	Femoral neck	6850	1.49	0.85
Gupta and Dan [22]	Apparent	<0.35	Scapulae	1050	2	0.403
		0.35–1.8		3000	3	0.987
Büchler et al. [23]	Apparent/1.8	n/r	n/r	15,000	2	n/r
Carter and Hayes [24]	Apparent	(0.18–2.00 rfg)	Human tibia and bovine femur	2875	3	n/r
Schaffler and Burr [32]	Ash	(0.644–0.723)<1.54	Bovine tibia and femur	60 + 900	2	n/r
	Apparent					
Rice et al. [25]	Apparent	(1.80–2.00)>1.54	Human and bovine	90	7.4	n/r
	Apparent					

Density range refers to piecewise density relationships. In brackets are the ranges of physical bone samples tested in the respective studies. Pooled values are from Vertebra (T10-L5), Proximal Tibia, Greater Trochanter, and Femoral Neck. The Büchler et al. [23] relationship is derived from Hayes [26], Reilly et al. [33], and Rice et al. [25] does not report which studies contributed to the relationships. Therefore, density range and anatomic location could not be extracted. Carter and Hayes [24] assume a physiologic strain rate of 0.01/s. n/r – not reported. rfg – read from graph.

applied element-wise, such that each element had a unique modulus assigned based on its corresponding voxel QCT density. The following equations derived from the co-registered VOIs were developed to convert QCT to apparent density. A linear relationship between the BV/TV of each μ-CT VOI and corresponding QCT density of each co-registered QCT VOI was used to develop Eq. (1). The relationship between BV/TV and apparent density described by Carter and Hayes [24] was then used to relate the QCT density to apparent density (Eq. (2)). This allowed Eq. (3) to be used to convert between QCT and apparent density and resulted in QCT-FEMs with a range of average apparent densities of 0.10 – 0.90 g/cm^3.

$$\rho_{QCT}\left[\frac{g_{K2HPO4}}{cm^3}\right] = 0.821\frac{BV}{TV} - 0.003 \tag{1}$$

$$\rho_{QCT}\left[\frac{g_{K2HPO4}}{cm^3}\right] = 0.821\frac{\rho_{app}}{1.8} - 0.003, \tag{2}$$

$$where\ \frac{BV}{TV} = \frac{\rho_{app}}{\rho_{real}},\ \text{with}\ \rho_{real} = 1.8\ \left[\frac{g}{cm^3}\right]\ [24]$$

$$\rho_{app}\left[\frac{g}{cm^3}\right] = 2.192\rho_{QCT} + 0.007 \tag{3}$$

For each QCT-FEM (6 × 98 = 588 models), the apparent strain energy density (SED_{app}) was calculated. The SED_{app} between QCT- and μ-FEMs were used to compare each density–modulus relationship's ability to map the apparent modulus to each virtual core (Fig. 1). To account for the larger number of cores than specimens, restricted maximum likelihood estimation (REML) linear regression fits were used (Matlab Statistics Toolbox, V. R2017a).

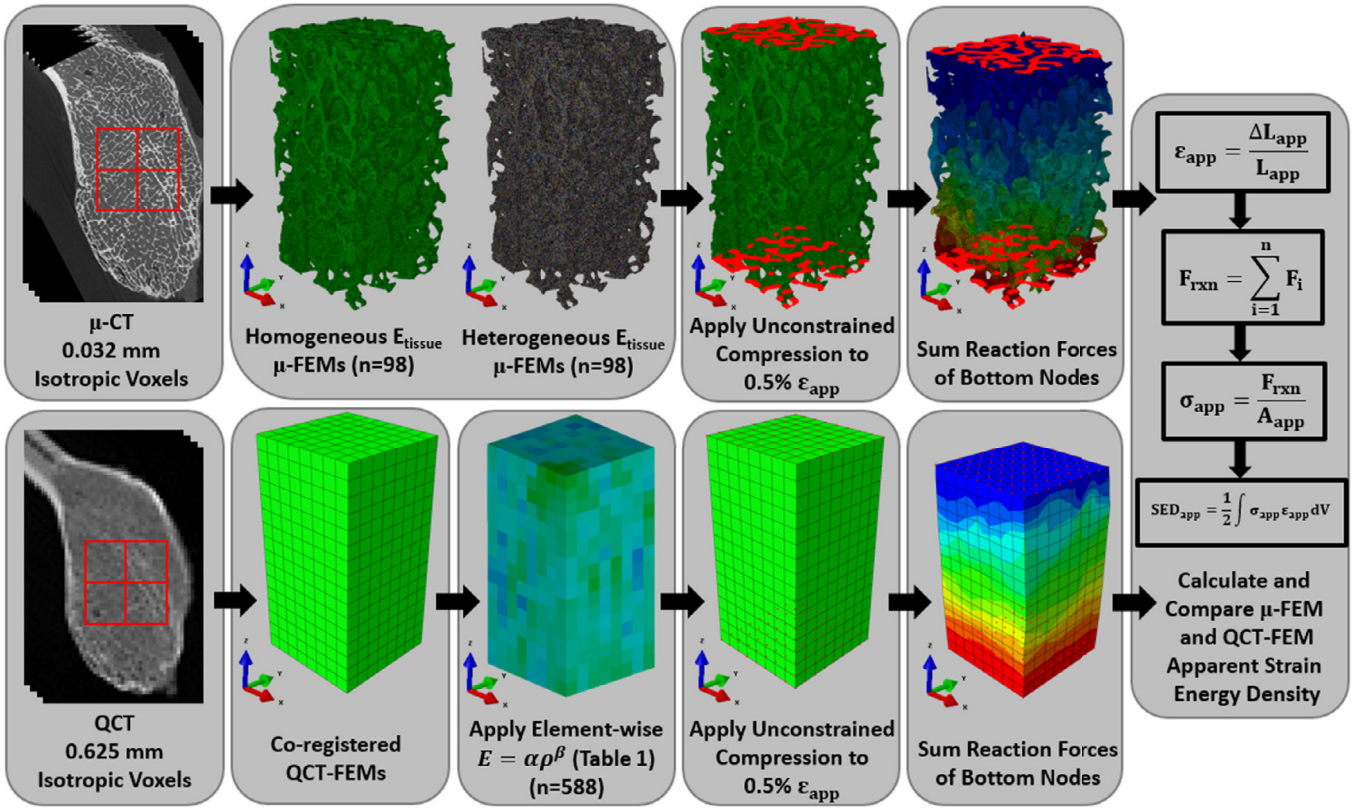

Fig. 1. The workflow used to create μ-FEMs and QCT-FEMs. Fourteen specimens were used to acquire μ-CT and QCT images. The μ-FEMs were applied either homogeneous (E_{tissue} = 20 GPa) or heterogeneous (E_{tissue} scaled by CT-intensity [13]), loaded in unconstrained compression and used to determine μ-FEMs apparent strain energy (SED_{app}). Co-registered QCT-FEMs were loaded with identical boundary conditions and the SED_{app} was compared to the μ-FEM SED_{app}.

Table 2
Results from restricted maximum likelihood estimation linear regression fits of apparent strain energy (SED_{app}) predictions between QCT-FEMs and homogeneous tissue modulus μ-FEMs (20 GPa).

QCT-FEM $SED_{app} = m$μ-FEM $SED_{app} + b$					
Author	r^2	m	b	SE	SE/mean (%)
Morgan et al. [21] – pooled	0.933	0.979	0.0066	0.0049	17.5
Morgan et al. [21] – femur	0.937	0.739	0.0098	0.0037	14.4
Gupta and Dan [22]	0.891	0.326	−0.0013	0.0019	32.2
Büchler et al. [23]	0.942	0.516	0.0021	0.0023	17.5
Carter and Hayes [24]	0.901	0.317	−0.0014	0.0017	31.7
Schaffler and Burr [32]	0.940	0.105	0.0013	0.0005	13.7
Rice et al. [25]					

r^2 – coefficient of determination; m – slope of regression line; b – intercept of regression line; SE – standard error of regression; SE/mean – standard error of regression as a percentage of the mean value.

3. Results

When considering comparisons between QCT-FEMs and μ-FEMs with a homogeneous tissue modulus, near absolute statistical agreement ($Y = X$) was observed between the μ-FEMs and the QCT-FEMs using the Morgan et al. [21] pooled relationship (Table 2). Not surprisingly, due to the similarity between the two relationships (Table 2), the Gupta and Dan [22] and Carter and Hayes [24] models showed near identical REML linear regression fit parameters. All relationships other than the Morgan et al. [21] pooled relationship, greatly underestimated the μ-FEM apparent strain energy density (SED_{app}) when considering a homogeneous tissue modulus in the μ-FEMs (Fig. 2). The Schaffler and Burr [32] and Rice et al. [25] relationship had the lowest standard error divided by the mean and the highest coefficient of determination, but greatly underestimated the μ-FEM SED_{app}. The underestimation of SED_{app} was also evident from the Bland–Altman plots for the homogeneous tissue modulus models. Significant proportional error for the Gupta and Dan [22], Carter and Hayes [24], the Schaffler and Burr [32], and Rice et al. [25] relationships was observed. There was also moderate proportional error for the Büchler et al. [23] relationship in these comparisons.

The same result with the pooled relationship did not hold true when the heterogeneous tissue modulus was considered in the μ-FEMs. The Büchler et al. [23] relationship most accurately predicted the SED_{app} for this comparison (Table 3). The Gupta and Dan [22] and Carter and Hayes [24] relationships again showed near identical REML linear regression fit parameters, and for the heterogeneous case, the Bland–Altman plots were nearly identical (Fig. 3). Again, the Schaffler and Burr [32] and Rice et al. [25] relationship had the lowest standard error divided by the mean and the highest coefficient of determination, but greatly underestimated the μ-FEM SED_{app}. The Bland–Altman proportional error illustrates an overestimation in SED_{app} with both Morgan et al. [21] relationships and proportional error underestimation of SED_{app} with the Schaffler and Burr [32] and Rice et al. [25] relationship.

4. Discussion

This study compared the six most commonly used density–modulus relationships used in finite element (FE) modeling of the shoulder using a computational methodology with co-registered μ-FEMs [16]. When a homogeneous effective tissue modulus is used in μ-FEMs the results suggest that density–modulus relationships mapped to co-registered QCT-FEMs pooled from multiple anatomic sites, may accurately predict the apparent strain energy density (SED_{app}) of glenoid trabecular bone. When considering a heterogeneous tissue modulus, the Büchler et al. [23] relationship most accurately predicted the SED_{app} of the μ-FEMs. The differences in SED_{app} between these two relationships and their ability to represent micro-level SED_{app} may be due to variations in the trabecular density range of the samples used in density–modulus relationship development and the resulting heterogeneity of the trabeculae.

The μ-FEMs used in this study were linear isotropic and therefore the arbitrary homogeneous effective tissue modulus can be scaled to determine the 'ideal' modulus for absolute statistical agreement ($Y = X$). In this case, the ideal effective tissue modulus for the Morgan et al. [21] pooled relationship was 20.43 GPa,

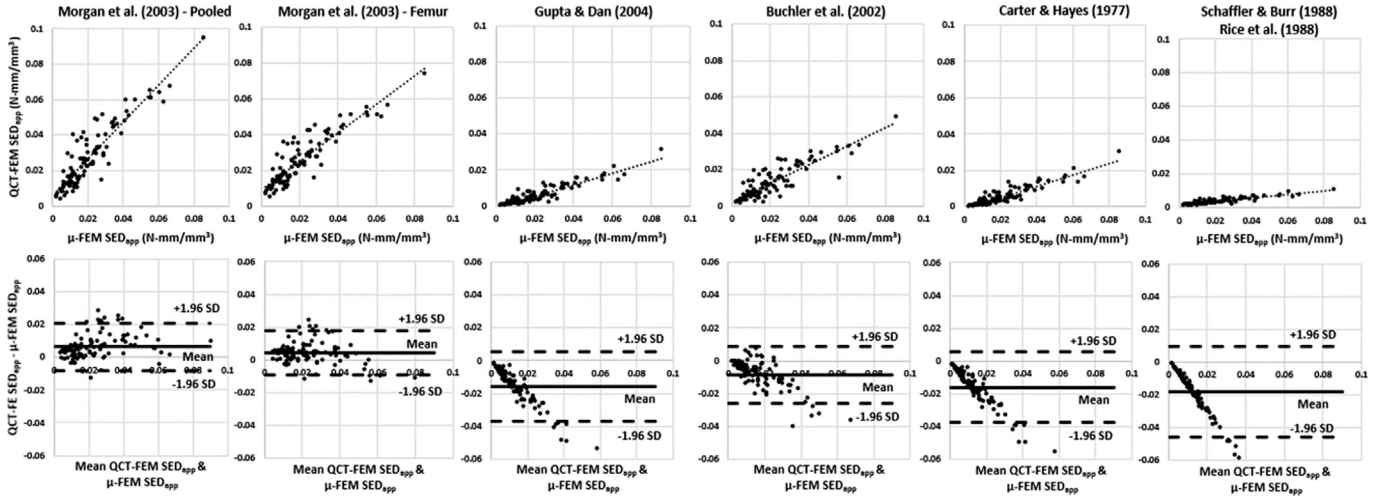

Fig. 2. Restricted maximum likelihood linear regression fits (upper row) and Bland–Altman plots (lower row) of the of the six density–modulus relationships compared for μ-FEM homogeneous tissue modulus of 20 GPa.

Table 3
Results from restricted maximum likelihood estimation linear regression fits of apparent strain energy (SED_{app}) predictions between QCT-FEMs and heterogeneous tissue modulus μ-FEMs.

QCT-FEM $SED_{app} = m$μ-FEM $SED_{app} + b$					
Author	r^2	m	b	SE	SE/mean (%)
Morgan et al. [21] – pooled	0.926	1.914	0.0091	0.0052	18.5
Morgan et al. [21] – femur	0.928	1.432	0.0119	0.0040	15.4
Gupta and Dan [22]	0.892	0.638	−0.0005	0.0019	32.2
Büchler et al. [23]	0.935	1.014	0.0034	0.0025	18.7
Carter and Hayes [24]	0.900	0.617	−0.0007	0.0018	32.2
Schaffler and Burr [32]	0.947	0.211	0.0015	0.0005	12.9
Rice et al. [25]					

Element-wise material heterogeneity in the μ-FEMs was applied to each model using a slope factor of 1.4 and a reference tissue modulus of 20 GPa [13]. r^2 – coefficient of determination; m – slope of regression line; b – intercept of regression line; SE – standard error of regression; SE/mean – standard error of regression as a percentage of the mean value.

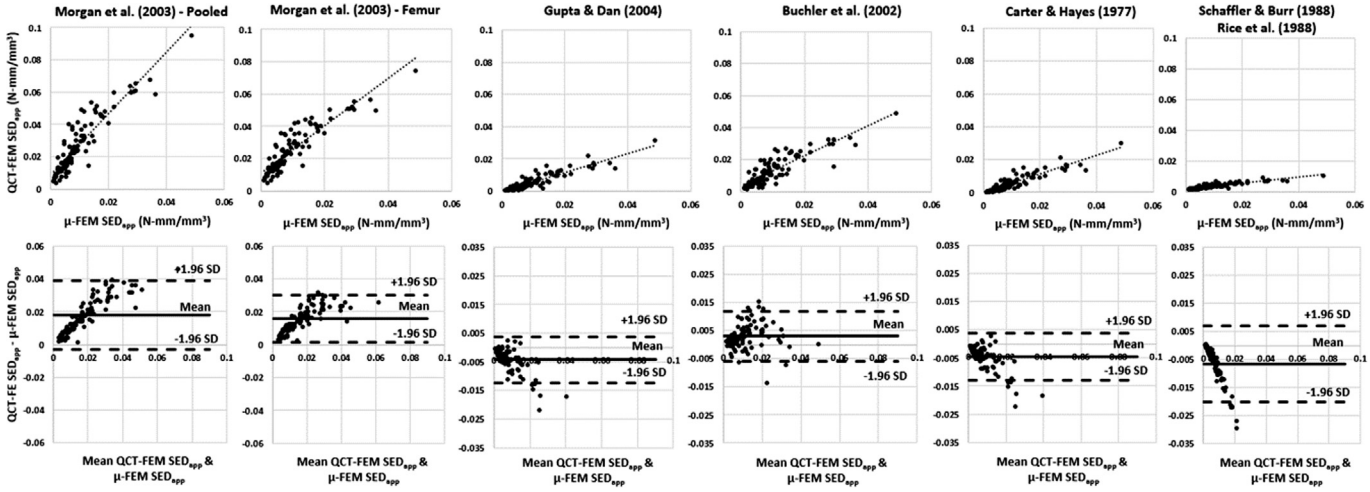

Fig. 3. Restricted maximum likelihood linear regression fits (upper row) and Bland–Altman plots (lower row) of the of the six density–modulus relationships compared for μ-FEM heterogeneous tissue modulus. The modulus was applied using a slope factor of 1.4 and a reference tissue modulus of 20 GPa [13].

which is consistent with the 20 GPa modulus chosen. Although Morgan et al. [21] do not report an effective tissue modulus for the pooled samples in their study, they do report an effective tissue modulus of 22 GPa for their relationship developed from femoral neck specimens. Our effective tissue modulus for this same relationship would be 27 GPa, when scaled to reach absolute statistical agreement. When translating micro-level mechanical property relationships to the apparent level, the apparent density is determined by the relationship between apparent modulus and apparent density. For accurate characterization among anatomic sites, this density range must be consistent because it is the only factor that is controlled in the density–modulus mapping to clinical-resolution derived FEMs.

Single anatomic site relationships are typically developed using an average density of a physical bone specimen, resulting in a relatively narrow range of density values. This is especially true in vertebrae, the greater trochanter, and the proximal tibia ($\rho_{app} = 0.09$–0.41) [21]. Anatomic sites that experience larger loads typically result in density values that extend to a larger range. When mapping density–modulus relationships derived from clinical-resolution scans, regardless of anatomic site, each voxel incorporates the full range of density values representative of bone, and therefore requires extrapolation beyond the typical range of average densities presented in many density–modulus relationships [7].

It is generally reported that due to variations in trabecular architecture and density by anatomic site, extrapolation beyond the presented density ranges and to alternative anatomic sites, is not recommended [7,21,34]. However, the apparent density ranges for the Morgan et al. [21] relationships (0.26–0.75 g/cm^3 for the femoral neck, and 0.09–0.75 g/cm^3 for pooled), were consistent with the apparent density range of the samples used in the present study (0.10–0.90 g/cm^3). Even though the density range is similar, these relationships ignore the variable contribution of trabecular architecture between anatomic sites. It has been reported that bone volume fraction (BV/TV) accounts for ∼90% of the elastic properties of trabecular bone, with architecture (based on fabric tensor) accounting for ∼10% [35]. Because BV/TV is inherently related to apparent density, this may indicate that a single density modulus relationship could accurately represent the mechanical properties of trabecular bone, independent of anatomic site. For this to hold true, the density range must be similar and anisotropy must be integrated into the QCT-FEMs. The integration of anisotropy into QCT-FEMs adds a level of complexity that is beyond the scope of many studies and has yet to be compared beyond the patella [36], femur [37], or tibia [38].

For the Büchler et al. [23] relationship the apparent density range for the samples used in the development of this relationship is unknown. However, it is possible that the heterogeneous tissue modulus of these samples more closely match the true heterogeneous distribution of the specimens tested in this study and may account for why this relationship was a stronger predictor of heterogeneous μ-FEMs SED_{app}. Load transfer paths are dependent not only on trabecular architecture, but also on the density of

individual trabeculae [9]. As such, multiple studies using experimental results for reference, have found that accounting for material heterogeneity in trabeculae improves the accuracy of μ-FEMs compared to homogeneous μ-FEMs [10–15]. The variation in mineralization across the width of trabeculae has significant influence on the bending stiffness, and as such may greatly alter the mechanical properties under compressive loading [12]. Due to this fact, it is not possible to scale the heterogeneous tissue modulus as with the homogeneous effective tissue modulus. Although the μ-FEM material mapping uses a linear mapping of tissue modulus based on CT-intensity, the distribution of CT-intensity varies by specimen, and the bending stresses are dependent on this tissue modulus distribution at the trabecular level.

The 'ideal' density–modulus relationship would result in absolute statistical agreement ($Y = X$) between μ-FEM and QCT-FEM SED_{app}, which was the primary metric for determining which relationship best mapped the mechanical properties to the QCT-FEMs. Although the Schaffler and Burr [32] and Rice et al. [25] relationship had the largest coefficient of determination (r^2) and lowest standard error of regression (SE), the proportional error shown in the Bland–Altman plots was largest for this relationship. The Morgan et al. [21] relationships showed similar coefficients of determination (r^2) and standard errors of regression (SE) for both the homogeneous (Table 2) and heterogeneous cases (Table 3) but had lower bias for the homogeneous case (Fig. 2), compared to the heterogeneous case (Fig. 3). If an effective homogeneous tissue modulus is assumed to accurately represent the tissue-level mechanical response of the trabecular bone, then the Morgan et al. [21] density–modulus relationship from pooled anatomic sites should be used. However, the perhaps more relevant heterogeneous tissue modulus case [10–15] indicates that the Büchler et al. [23] density–modulus relationship should be used to model trabecular bone in shoulder FEMs.

A limitation of this study is that physical bone specimens were not directly tested. The wide variety of testing protocols that are reported in density–modulus relationship development [7] provides a confounding bias that is difficult to account for when testing the mapping of constitutive relationships. Although physical bone specimen testing has become the 'gold standard' in density–modulus relationship development, recent literature has shown excellent correlations of μ-FEMs with empirical data [17,39], indicating that μ-FEMs can accurately determine the apparent mechanical properties of trabecular bone without the need for empirical mechanical testing. The computational methodology used in this study [16] eliminates the systematic error resulting from specimen preparation, end-artifacts, physical measurement error, and stiffness variations that may occur in testing apparatus. This methodology allows for an indirect comparison and determination of the most accurate density–modulus relationships, as suggested by Helgason et al. [7]. To provide external validation with these comparisons, empirical modeling could be combined with μ-FEM development. These models should replicate empirical boundary conditions using digital volume correlation (DVC) and compare full-field DVC results to computational results [17]. Further studies should be performed to determine whether these relationships can be translated to whole bones. This may provide insight into the predictive capabilities of using pooled or custom density–modulus relationships in the mapping of mechanical properties in future clinical-resolution derived FEMs of the shoulder.

Acknowledgments

The authors would like to thank Shruthi Poolacherla for her assistance with data collection. Funding for this work was provided in part by a Lawson Health Research Internal Research Fund Grant. Nikolas K. Knowles is supported in part by the Natural Sciences and Engineering Research Council of Canada and by a Transdisciplinary Bone & Joint Training Award from the Collaborative Training Program in Musculoskeletal Health Research at The University of Western Ontario. Ethics approval was obtained from the University of Western Ontario Health Sciences Research Ethics Board (HSREB) file #105912.

Conflict of interest

The authors have no conflict of interest with this work.

References

[1] Dahan G, Trabelsi N, Safran O, Yosibash Z. Verified and validated finite element analyses of humeri. J Biomech 2016;49:1094–102. doi:10.1016/j.jbiomech.2016.02.036.
[2] Knowles NK, Reeves JM, Ferreira LM. Quantitative Computed Tomography (QCT) derived Bone Mineral Density (BMD) in finite element studies: a review of the literature. J Exp Orthop 2016;3:36. doi:10.1186/s40634-016-0072-2.
[3] Unnikrishnan GU, Barest GD, Berry DB, Hussein AI, Morgan EF. Effect of specimen-specific anisotropic material properties in quantitative computed tomography-based finite element analysis of the vertebra. J Biomech Eng 2013;135:101007–11. doi:10.1115/1.4025179.
[4] Schileo E, Dall'Ara E, Taddei F. An accurate estimation of bone density improves the accuracy of subject-specific finite element models. J Biomech 2008;41(11):2483–91.
[5] Schileo E, Taddei F, Malandrino A, Cristofolini L, Viceconti M. Subject-specific finite element models can accurately predict strain levels in long bones. J Biomech 2007;40:2982–9. doi:10.1016/j.jbiomech.2007.02.010.
[6] Campoli G, Weinans H, van der Helm F, Zadpoor Aa. Subject-specific modeling of the scapula bone tissue adaptation. J Biomech 2013;46:2434–41. doi:10.1016/j.jbiomech.2013.07.024.
[7] Helgason B, Perilli E, Schileo E, Taddei F. Mathematical relationships between bone density and mechanical properties: a literature review. Clin Biomech 2008;23:135–46. doi:10.1016/j.clinbiomech.2007.08.024.
[8] Bayraktar HH, Morgan EF, Niebur GL, Morris GE, Wong EK, Keaveny TM. Comparison of the elastic and yield properties of human femoral trabecular and cortical bone tissue. J Biomech 2004;37:27–35. doi:10.1016/S0021-9290(03)00257-4.
[9] Ün K, Bevill G, Keaveny TM. The effects of side-artifacts on the elastic modulus of trabecular bone. J Biomech 2006;39:1955–63. doi:10.1016/j.jbiomech.2006.05.012.
[10] Jaasma MJ, Bayraktar HH, Niebur GL, Keaveny TM. Biomechanical effects of intraspecimen variations in tissue modulus for trabecular bone. J Biomech 2002;35:237–46. doi:10.1016/S0021-9290(01)00193-2.
[11] Renders GAP, Mulder L, Langenbach GEJ, van Ruijven LJ, van Eijden TMGJ. Biomechanical effect of mineral heterogeneity in trabecular bone. J Biomech 2008;41:2793–8. doi:10.1016/j.jbiomech.2008.07.009.
[12] Renders GAP, Mulder L, van Ruijven LJ, Langenbach GEJ, van Eijden TMGJ. Mineral heterogeneity affects predictions of intratrabecular stress and strain. J Biomech 2011;44:402–7. doi:10.1016/j.jbiomech.2010.10.004.
[13] Bourne BC, Van Der Meulen MCH. Finite element models predict cancellous apparent modulus when tissue modulus is scaled from specimen CT-attenuation. J Biomech 2004;37:613–21. doi:10.1016/j.jbiomech.2003.10.002.
[14] van Ruijven LJ, Mulder L, van Eijden TMGJ. Variations in mineralization affect the stress and strain distributions in cortical and trabecular bone. J Biomech 2007;40:1211–18. doi:10.1016/j.jbiomech.2006.06.004.
[15] Harrison NM, McDonnell PF, O'Mahoney DC, Kennedy OD, O'Brien FJ, McHugh PE. Heterogeneous linear elastic trabecular bone modelling using micro-CT attenuation data and experimentally measured heterogeneous tissue properties. J Biomech 2008;41:2589–96. doi:10.1016/j.jbiomech.2008.05.014.
[16] Knowles NK, Langohr GDG, Faieghi M, Nelson A. Development of a validated glenoid trabecular density–modulus relationship. J Mech Behav Biomed Mater 2019;90:140–5. doi:10.1016/j.jmbbm.2018.10.013.
[17] Chen Y, Dall'Ara E, Sales E, Manda K, Wallace R, Pankaj P, et al. Micro-CT based finite element models of cancellous bone predict accurately displacement once the boundary condition is well replicated: a validation study. J Mech Behav Biomed Mater 2017;65:644–51. doi:10.1016/j.jmbbm.2016.09.014.
[18] Podshivalov L, Fischer A, Bar-Yoseph PZ. 3D hierarchical geometric modeling and multiscale FE analysis as a base for individualized medical diagnosis of bone structure. Bone 2011;48:693–703. doi:10.1016/j.bone.2010.12.022.
[19] Brennan O, Kennedy OD, Lee TC, Rackard SM, O'Brien FJ. Biomechanical properties across trabeculae from the proximal femur of normal and ovariectomised sheep. J Biomech 2009;42:498–503. doi:10.1016/j.jbiomech.2008.11.032.
[20] Oftadeh R, Perez-Viloria M, Villa-Camacho JC, Vaziri A, Nazarian A. Biomechanics and mechanobiology of trabecular bone: a review. J Biomech Eng 2015;137:10802. doi:10.1115/1.4029176.
[21] Morgan E, Bayraktar H, Keaveny T. Trabecular bone modulus–density relationships depend on anatomic site. J Biomech 2003;36(7):897–904.
[22] Gupta S, Dan P. Bone geometry and mechanical properties of the human scapula using computed tomography data. Trends Biomater Artif Organs 2004;17:61–70.

[23] Büchler P, Ramaniraka NA, Rakotomanana LR, Iannotti JP, Farron A. A finite element model of the shoulder: application to the comparison of normal and osteoarthritic joints. Clin Biomech 2002;17:630–9. doi:10.1016/S0268-0033(02)00106-7.
[24] Carter D, Hayes W. The compressive behavior of bone as a two-phase porous structure. J Bone Jt Surg 1977;59(7):954–62.
[25] Rice J, Cowin S, Bowman J. On the dependence of the elasticity and strength of cancellous bone on apparent density. J Biomech 1988;21(2):155–68.
[26] Hayes WC. Biomechanics of cortical and tubecular bone: implications for assessment of fracture risk. New York: Raven Press; 1991. Basic Orthop. Biomech. p. 93–142.
[27] Guldberg RE, Hollister SJ, Charras GT. The accuracy of digital image-based finite element models. J Biomech Eng 1998;120:289. doi:10.1115/1.2798314.
[28] Niebur GL, Yuen JC, Hsia AC, Keaveny TM. Convergence behavior of high-resolution finite element models of trabecular bone. J Biomech Eng 1999;121:629. doi:10.1115/1.2800865.
[29] Bouxsein ML, Boyd SK, Christiansen BA, Guldberg RE, Jepsen KJ, Müller R. Guidelines for assessment of bone microstructure in rodents using micro-computed tomography. J Bone Miner Res 2010;25:1468–86. doi:10.1002/jbmr.141.
[30] Faieghi M, Knowles NK, Tutunea-fatan OR, Ferreira LM. Fast generation of Cartesian meshes from micro-computed tomography data. Comput Aided Des Appl 2019;16:161–71.
[31] Morgan EF, Keaveny TM. Dependence of yield strain of human trabecular bone on anatomic site. J Biomech 2001;34:569–77.
[32] Schaffler MB, Burr DB. Stiffness of compact bone: effects of porosity and density. J. Biomech. 1988;21(1):13–16.
[33] Reilly DT, Burstein AH, Frankel VH. The elastic modulus for bone. J. Biomech. 1974;7(3):271–5.
[34] Kopperdahl DL, Morgan EF, Keaveny TM. Quantitative computed tomography estimates of the mechanical properties of human vertebral trabecular bone. J Orthop Res 2002;20:801–5. doi:10.1016/S0736-0266(01)00185-1.
[35] Maquer G, Musy SN, Wandel J, Gross T, Zysset PK. Bone volume fraction and fabric anisotropy are better determinants of trabecular bone stiffness than other morphological variables. J Bone Miner Res 2015;30:1000–8. doi:10.1002/jbmr.2437.
[36] Latypova A, Maquer G, Elankumaran K, Pahr D, Zysset P, Pioletti DP, et al. Identification of elastic properties of human patellae using micro-finite element analysis. J Biomech 2016;49:3111–15. doi:10.1016/j.jbiomech.2016.07.031.
[37] Enns-Bray WS, Ariza O, Gilchrist S, Widmer Soyka RP, Vogt PJ, Palsson H, et al. Morphology based anisotropic finite element models of the proximal femur validated with experimental data. Med Eng Phys 2016;38:1339–47. doi:10.1016/j.medengphy.2016.08.010.
[38] Nazemi SM, Kalajahi SMH, Cooper DML, Kontulainen SA, Holdsworth DW, Masri BA, et al. Accounting for spatial variation of trabecular anisotropy with subject-specific finite element modeling moderately improves predictions of local subchondral bone stiffness at the proximal tibia. J Biomech 2017;59:101–8. doi:10.1016/j.jbiomech.2017.05.018.
[39] Costa MC, Tozzi G, Cristofolini L, Danesi V, Viceconti M, Dall'Ara E. Micro finite element models of the vertebral body: validation of local displacement predictions. PLoS One 2017;12:1–18. doi:10.1371/journal.pone.0180151.